

Methodology for determining the electronic thermal conductivity of metals via direct non-equilibrium ab initio molecular dynamics

Sheng-Ying Yue,¹ Xiaoliang Zhang,² Stephen Stackhouse,³ Guangzhao Qin,² Edoardo Di Napoli,^{1,4} and Ming Hu^{1,2,*}

¹*Aachen Institute for Advanced Study in Computational Engineering Science (AICES),
RWTH Aachen University, 52062 Aachen, Germany*

²*Institute of Mineral Engineering, Division of Materials Science and Engineering,
Faculty of Georesources and Materials Engineering,
RWTH Aachen University, 52064 Aachen, Germany*

³*School of Earth and Environment, University of Leeds, Leeds LS2 9JT, United Kingdom*

⁴*Jülich Supercomputing Centre, Forschungszentrum Jülich and JARA-HPC, 52425 Jülich, Germany*

Many physical properties of metals can be understood in terms of the free electron model [1], as proven by the Wiedemann-Franz law [2]. According to this model, electronic thermal conductivity (κ_{el}) can be inferred from the Boltzmann transport equation (BTE). However, the BTE does not perform well for some complex metals, such as Cu. Moreover, the BTE cannot clearly describe the origin of the thermal energy carried by electrons or how this energy is transported in metals. The charge distribution of conduction electrons in metals is known to reflect the electrostatic potential (EP) of the ion cores [1]. Based on this premise, we develop a new methodology for evaluating κ_{el} by combining the free electron model and non-equilibrium ab initio molecular dynamics (NEAIMD) simulations. We demonstrate that the kinetic energy of thermally excited electrons originates from the energy of the spatial electrostatic potential oscillation (EPO), which is induced by the thermal motion of ion cores. This method directly predicts the κ_{el} of pure metals with a high degree of accuracy.

κ_{el} is one of the most important physical properties of metals. The analytical solution of κ_{el} based on the BTE and free electron model can be expressed as

$$\kappa_{el} = \frac{\pi^2 n k_B^2 T \tau_{el}}{3m}, \quad (1)$$

where n is the concentration of free electrons, m is the electron mass, k_B is the Boltzmann constant, T is the system temperature and τ_{el} is the collision time of free electrons, which is mainly determined by electron-electron, electron-hole and electron-phonon scattering. In principle, we can obtain an approximate value for τ_{el} from Matthiessen's rule. However, describing every scattering process involved in the heat transfer by electrons of solid metals is too complicated. Recently, several methods have been reported for the evaluation of the electronic thermal conductivities of liquid-phase metals within the framework of density functional theory (DFT),

such as ab initio molecular dynamics (AIMD) using the Kubo-Greenwood equation [3–5] and DFT plus dynamical mean-field theory (DFT+DMFT) [6].

In this paper, we develop a new methodology to describe the electronic heat-transport process in solid metals without explicitly addressing detailed scattering processes. From the second law of thermodynamics, we know that heat transfer in solids is driven by the temperature gradient ∇T . Typically, temperature describes the thermal motion of atoms, and the vibrations of ions can lead to spatial EPO, as can be easily deduced from the mathematical expression for the total Hamiltonian of system. Local variation of the EP can drive the collective oscillation of free electrons, and those free electrons near the Fermi surface can be excited above the Fermi surface and obtain additional thermal kinetic energy with respect to 0 K. These are called thermally excited electrons. Figs. 1(a, b) show two cartoons describing how the thermally excited electrons move in the vibrational lattice and the local EP field. Higher temperatures, which induce larger and faster ionic vibrations, lead to stronger EPO. Thus, the thermally excited electrons in high-temperature regions have more kinetic energy than those in low-temperature regions. Once a stable distribution of the thermal kinetic energy of thermally excited electrons is established along the direction of ∇T , then the heat flux carried by thermally excited electrons and κ_{el} can be calculated.

To prove this conjecture and quantify κ_{el} , we performed NEAIMD simulations [7, 8] by modifying the Vienna Ab initio Simulation Package (VASP) [9, 10]. The atomic heat flux was realized using the Müller-Plathe algorithm [11], in which the kinetic energies of the atoms in the heat source and heat sink are exchanged (Supplementary Information (SI) Sec. 1). With sufficient simulation time, we can establish a stable temperature gradient in metals. Figs. 1(c, d) present the Cu model and the corresponding temperature profile, respectively. Simultaneously, we can calculate the spatial distribution and the dynamical evolution of the EP, which is expressed as

$$U = \int U(r) \cdot \rho_{\text{test}} \cdot (|r - R|) d^3r, \quad (2)$$

where the test charge ρ_{test} is the norm 1, and R represents the ion position. Fig. 1(e) shows the theoretical

*Electronic address: hum@ghi.rwth-aachen.de

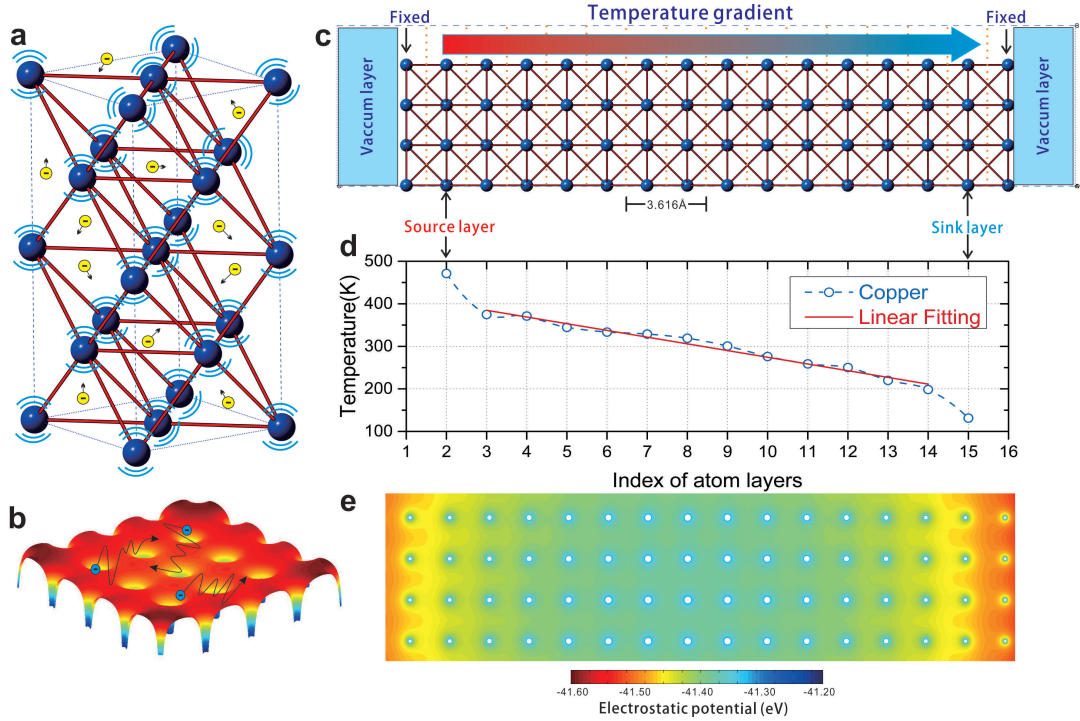


FIG. 1: Overview of the simulation model, temperature profile and EP field of copper. **a, b**, Cartoons of free electrons in a metal moving in the vibrating lattice and EP field. **c, d**, Model of copper used in NEAIMD simulations and the corresponding temperature profile. One unit cell length comprises two layers of atoms. We use fixed boundary conditions with the layers of fixed atoms and vacuum layers along the direction of ∇T . Periodic boundary conditions are adopted in the other two dimensions. **e**, Theoretical EP field of a perfect copper structure (the test charge number is norm 1).

results of the static distribution of the EP for a perfect Cu lattice. In the rest of this paper, we 1) illustrate the relationship between the spatial EPO and lattice vibrations, 2) demonstrate that the EPO provides additional kinetic energy to thermally excited electrons, and 3) show how to predict κ_{el} within our theoretical framework.

To demonstrate the relationship between EPO and lattice vibrations, we analyse the data from our AIMD simulations using the power spectral density (PSD) method [12, 13]. For a stationary signal $x(t)$, the PSD is defined as

$$S_x(f) = \int_{-\infty}^{\infty} R_x(\tau) e^{-2\pi i f \tau} d\tau, \quad (3)$$

where $R_x(\tau) = E[x(t)x(t+\tau)]$ is the autocorrelation function of $x(t)$ [12, 13], and $E[\cdot]$ denotes the expectation value. Here, we consider four signals from an AIMD simulation: atomic displacement D_{ion} , atomic velocity V_{ion} , EP displacement U_{ion} , and velocity of EPO (VEPO) ΔU_{ion} ; these are used to calculate their respective spectral densities S_D , S_V [14], S_U , $S_{\Delta U}$ (SI Sec. 2). S_D and S_V reflect the frequency-dependent lattice vibrations at a specific T . Analogously, S_U and $S_{\Delta U}$ provide information regarding the EPO with respect to frequency. We show results for Al from a 10-ps equilibrium AIMD run at 100.90 K (Figs. 2(a, b)) and a 70-ps NEAIMD simulation at 299.46 K (Figs. 2(c, d)). Fig. 2(a)

clearly shows that the locations of the density peaks of S_D and S_U are consistent, demonstrating that the EPO is mainly caused by the lattice vibration of ion cores. Fig. 2(b) confirms this relationship. Similar results are shown in Figs. 2(c, d): for most of the frequency ranges, the peaks of S_D and S_U , S_V and $S_{\Delta U}$ are consistent with each other. However, for some specific frequencies in Figs. 2(c, d) (3.5 ~ 5.0 THz), some discrepancies exist in the peaks' magnitudes. This phenomenon may be attributable to the heat flux applied in the NEAIMD simulations. Nevertheless, Figs. 2(a ~ d) provide unambiguous evidence that the EPO is directly induced by the lattice vibration of ions in metals.

To understand the dynamical evolution of spatial EPO intuitively, we present the representative case of Cu, calculated using NEAIMD at 298.49 K, in Fig. 2(e). Little variation occurs in the local electronic field between neighbouring atom layers, and the directions of these local fields continually change with time. The variations of these local fields will drive the collective vibration of free electrons, as theoretically illustrated in Fig. 2(f). We see that only free electrons near the Fermi surface can be thermally excited. Because the direction of the local field continually changes with time, the vectors of the local momentum of the thermally excited electrons should also continually change with time. Therefore, for a sufficiently long statistical time average, no net electric

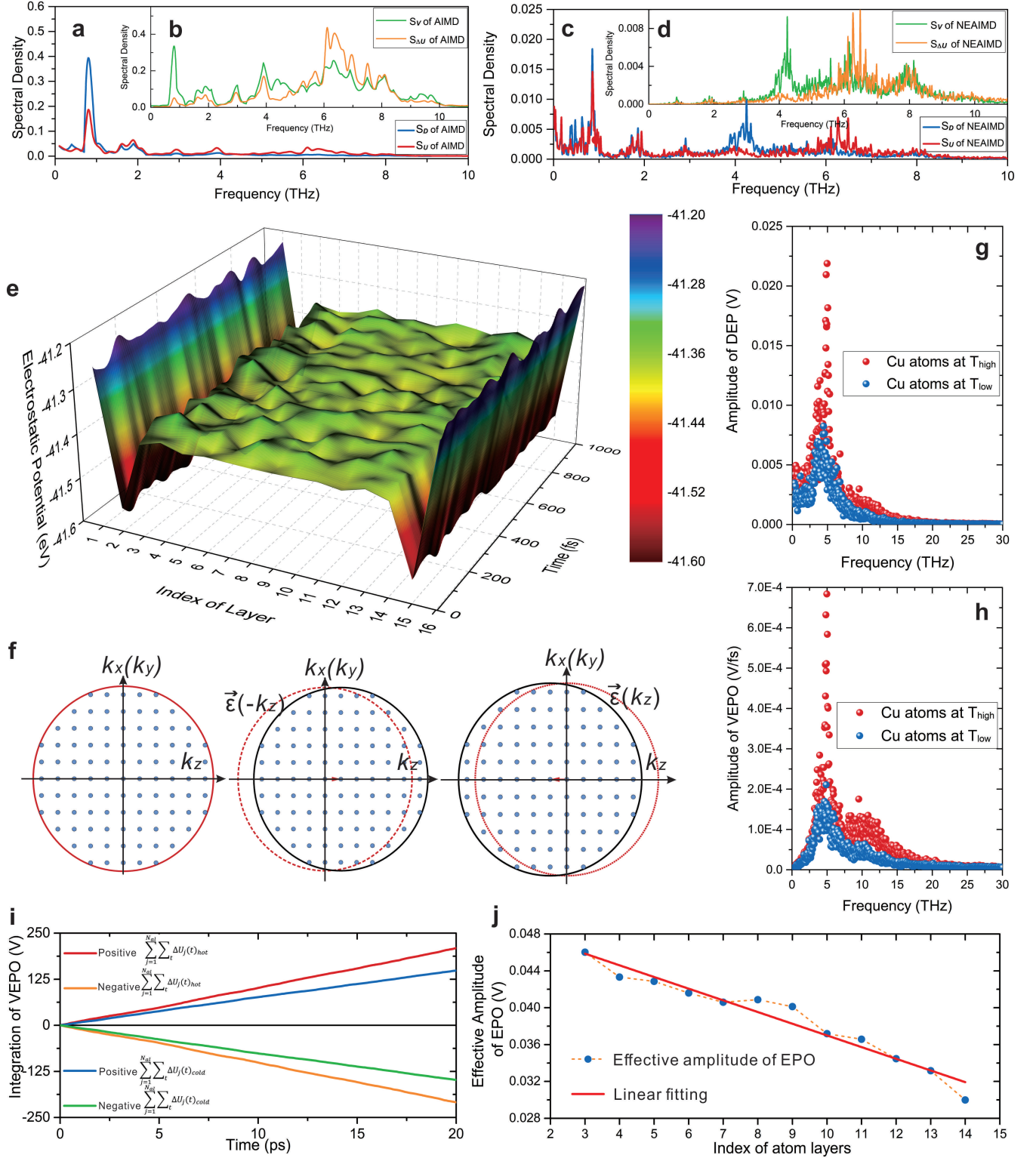


FIG. 2: Overview of the relationship between EPO at ion cores and lattice vibrations. **a, c**, Blue and red lines, represent the spectral density of atom displacements (S_D) and the EP displacement (S_U) at specific ion cores. **b, d**, Green and orange lines, represent the spectral density of atom velocities (S_V) and the EPO velocities ($S_{\Delta U}$), respectively, at specific ion cores. Data in **(a, b)** are from a 10-ps equilibrium AIMD simulation of Al at 100.90 K, whereas **(c, d)** present the same physical quantities from a 70-ps NEAIMD simulation of Al at 299.46 K. Data shown in **(e, g-j)** are from a 20-ps NEAIMD simulation of Cu at 298.49 K. **e**, The variation of EPO in space over time (the test charge number is 1). **f**, Schematic of the whole Fermi sphere oscillation as local electric field vibration along the \vec{z} direction. **g, h**, The direct fast Fourier transform (FFT) amplitudes of the displacement of EP (DEP, U_{ion}) and VEPO (ΔU_{ion}) of ion cores at different temperatures. **i**, Integration of positive and negative VEPO ($\sum_{j=1}^{N_{al}} \sum_t \Delta U_j(t)$) at different temperatures. **j**, The effective amplitude of EPO ($\frac{1}{N_{al}} \sum_{j=1}^{N_{al}} \sqrt{\frac{1}{n_{steps}} \sum_{i=1}^{n_{steps}} (U_{ij} - \bar{U}_j)^2}$, average root mean square (RMS) [15] of EPO, where N_{al} is the atom number per layer) in atom layers along the \vec{z} direction.

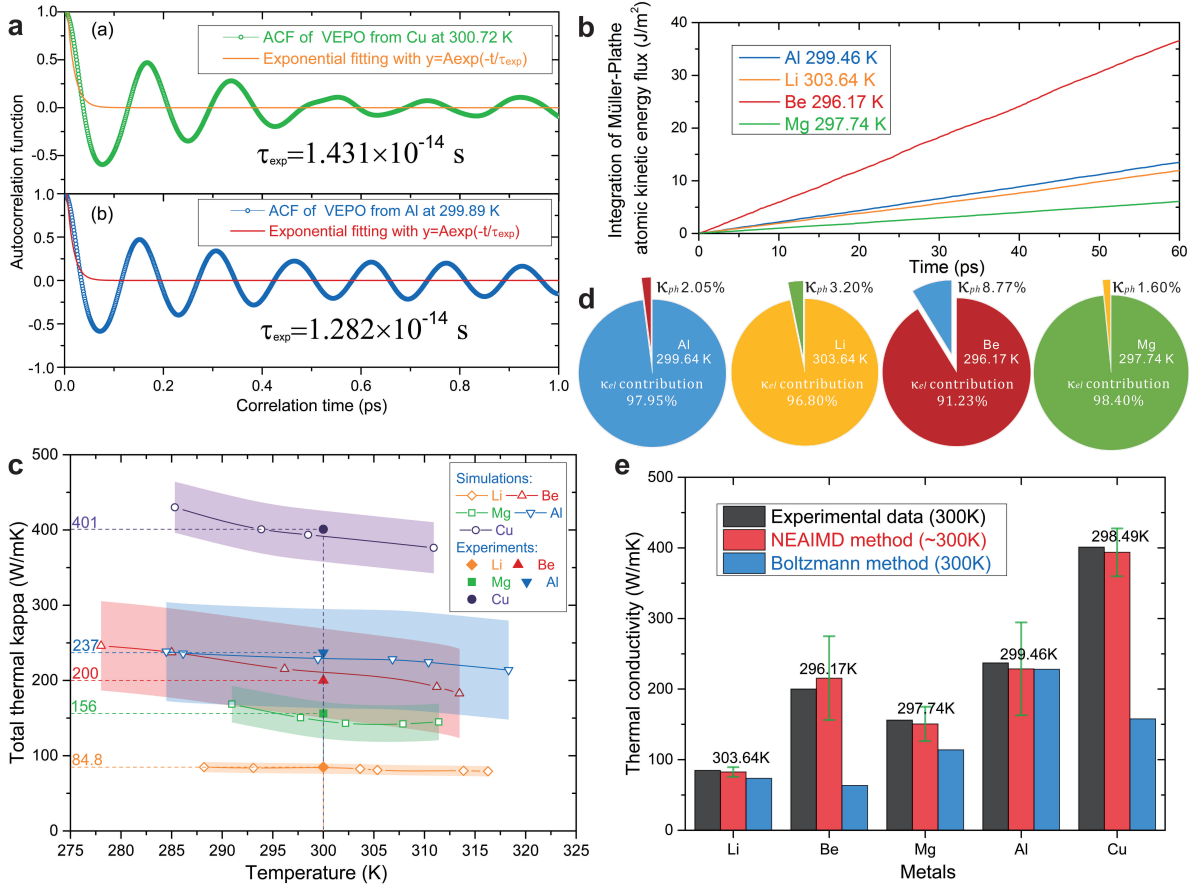


FIG. 3: NEAIMD-EPO simulation results for metals. **a**, Autocorrelation function of VEPO from Cu and Al NEAIMD simulations. The exponential fitting followed the function: $y = A \exp(-t/\tau_{\text{exp}})$, where τ_{exp} represents the exponential autocorrelation time of VEPO. **b**, Integration of the atomic kinetic energy flux with time based on the NEAIMD (Müller-Plathe) simulations of Al, Li, Be and Mg. **c**, Total thermal conductivities of metals from NEAIMD simulation (with error bars determined from the calculation of ∇T and $\frac{\partial \bar{U}_{EPO}(l)}{\partial N_l}$ along the heat-transport direction) and experimental data at 300 K. **d**, Pie graphs showing the electronic and phononic contributions to the total thermal conductivity of Al, Li, Be, and Mg. **e**, Bar graph comparing the thermal conductivities of metals calculated using the NEAIMD method (with error bars), Boltzmann method and experimental data at 300 K.

current should arise during the thermal transport process of metals. This is consistent with the traditional free electron model [1].

To prove that the EPO provides additional kinetic energy to thermally excited electrons in metals, we run a 100-ps equilibrium AIMD for Al at 329.40 K and Li at 283.97 K (both with a $2 \times 2 \times 2$ conventional-cell and 32 total atoms). When $T > 0$ K, the total energy of the free electron system can be written as [1, 2](SI Sec. 3)

$$E_{\text{sys}} = E_0 + E_T = E_0 + \frac{\pi^2}{4} \cdot N \frac{(k_B T)^2}{E_F^0},$$

where E_0 is the total energy of the free electron system at 0 K, E_T is the thermally excited energy of the free electron system obtained from the outside environment when $T > 0$ K, N is the total number of free electrons, and E_F^0 is the Fermi energy at 0 K. We also calculate the

energy provided by EPO using

$$E_{EPO} = 2 \cdot \bar{U}_{EPO} \cdot N \cdot e,$$

where \bar{U}_{EPO} is the average effective EPO amplitude. For Al, $E_T = 2.6293 \times 10^{-21}$ J and $E_{EPO} = 2.7674 \times 10^{-21}$ J. For Li, $E_T = 1.6049 \times 10^{-21}$ J and $E_{EPO} = 1.5909 \times 10^{-21}$ J. From these results, we have

$$E_T \approx E_{EPO}. \quad (4)$$

We conclude that lattice vibrations cause EPO in metals, and simultaneously, EPO drives the collective vibration of free electrons. The energy of these collective vibrations provides additional kinetic energy to the thermally excited electrons. This is the core concept underlying this methodology.

Within this theoretical framework, higher temperatures strengthen the spatial EPO. To prove this relationship, we perform direct FFT of the relative displacement

of EP U_{ion} and VEPO ΔU_{ion} . U_{ion} and ΔU_{ion} were used to calculate S_U and $S_{\Delta U}$ in Figs. 2(a – d). U_{ion} describes the strength of the EPO in space, whereas ΔU_{ion} reflects how fast the oscillation changes. Figs. 2(g, h) show the frequency-dependent FFT amplitudes of U_{ion} and ΔU_{ion} , respectively. Clearly, the EPO is stronger and faster at higher temperatures.

In Fig. 2(i), we present the positive and negative integrations of the total ΔU_{ion} in the same atom layer with simulation time, which can be written as $\sum_{j=1}^{N_{\text{al}}} \sum_t \Delta U_j(t)$, where j is the index of the atom in the layer and N_{al} is the total number of atoms per layer. The four quantities in Fig. 2(i) show perfect linear behaviour over time. From the absolute values, we have:

$$\sum_{j=1}^{N_{\text{al}}} \sum_t |\Delta U_j(t)_{\text{hot}}| > \sum_{j=1}^{N_{\text{al}}} \sum_t |\Delta U_j(t)_{\text{cold}}|,$$

which is consistent with the evidence shown in Figs. 2(g, h). Notably, in the same temperature region, the positive and negative accumulations of $\sum_{j=1}^{N_{\text{al}}} \Delta U_j(t)$ are almost the same. In other words, $\sum_{j=1}^{N_{\text{al}}} \sum_t \Delta U_j(t) \simeq 0$, and thus, there is no net electric field gradient along the heat flux direction for a sufficiently long statistical time. This result confirms the physical picture illustrated in Fig. 2(f). Fig. 2(j) presents the distribution of the average effective amplitude of EPO in each atom layer along the heat flux direction, $\bar{U}_{\text{EPO}}(l)$, where l is the index of the atom layers. Moreover, the amplitude distribution of EPO explains how the thermal kinetic energy of thermally excited electrons is divided in space. We calculate $\bar{U}_{\text{EPO}}(l)$ using the RMS method [15]:

$$\bar{U}_{\text{EPO}}(l) = \frac{1}{N_{\text{al}}} \sum_{j=1}^{N_{\text{al}}} \sqrt{\frac{1}{n_{\text{steps}}} \sum_{t_i}^{n_{\text{steps}}} (U_j(t_i) - \bar{U}_j)^2},$$

where n_{steps} is the total number of simulation time steps, $U_j(t_i)$ is the U value of atom j in a specific layer at time step t_i , and \bar{U}_j is the average value of $U_j(t_i)$. Then, we define the heat flux of electrons \vec{J}_{el} according to the kinetic energy of thermally excited electrons between two adjacent atom layers. Because of the isotropy of the free electron model (SI Sec. 4), we take half of the difference of the thermal kinetic energy of thermally excited electrons between the two layers as

$$\begin{aligned} \vec{J}_{\text{el}} &= -\frac{1}{2} \frac{n(e) \cdot e \cdot \partial[2 \cdot \bar{U}_{\text{EPO}}(l) \cdot n_{\text{steps}}]}{S \cdot t \cdot \partial N_l} \\ &= -\frac{n(e) \cdot e \cdot n_{\text{steps}}}{S \cdot t} \frac{\partial \bar{U}_{\text{EPO}}(l)}{\partial N_l}, \end{aligned} \quad (5)$$

where S is the cross-sectional area, t is the total simulation time, $n(e)$ is the number of free electrons per atom layer, and $\frac{\partial \bar{U}_{\text{EPO}}(l)}{\partial N_l}$ is the gradient of the average effective amplitude value of EPO by linear fitting of $\bar{U}_{\text{EPO}}(l)$ with the atom layer index number N_l shown in Fig. 2(j). Here,

a nonlinear phenomenon exists in the effective EPO amplitude distribution along the heat flux direction in some metals, such as Al, Be, and Mg. According to a case study of Be, we find that the nonlinear effect of $\bar{U}_{\text{EPO}}(l)$ can be reduced by increasing the system size (SI Sec. 4.2). Because of the nonlinear effect, when we calculate the \vec{J}_{el} of Al, Be and Mg, we fit the linear part only. For Cu and Li, the $\bar{U}_{\text{EPO}}(l)$ distributions exhibit perfect linear behaviour along the heat current direction. Thus, we can calculate κ_{el} based on Fourier's law:

$$\vec{J} = -\kappa \nabla T. \quad (6)$$

Combining Eqs. (5, 6), we obtain the expression for κ_{el} :

$$\kappa_{\text{el}} = \frac{n(e) \cdot e \cdot n_{\text{steps}}}{\nabla T \cdot S \cdot t} \frac{\partial \bar{U}_{\text{EPO}}(l)}{\partial N_l}, \quad (7)$$

where ∇T is obtained by linear fitting the temperature profile with the representative case shown in Fig. 1(d).

Within this framework, we studied the κ_{el} of five metals (Li, Be, Mg, Al, and Cu) near room temperature. Additionally, by integrating the Müller-Plathe [11] atomic kinetic energy flux, as shown in Fig. 3(b), we predict the lattice (phonon) thermal conductivities of the metals (κ_{ph}). Because of finite size effects, our NEAIMD results underestimate κ_{ph} , especially for Cu and Mg (SI Sec. 5). By summing κ_{el} and κ_{ph} from the NEAIMD simulations, we obtain the total thermal conductivities of the metals, as presented in Fig. 3(c). The results demonstrate that the thermal conductivities of metals slowly decrease with temperature near room temperature, which is consistent with traditional theory and experimental data. The error estimates in Fig. 3(c) are calculated from the expression for κ_{el} and error propagation theory [16]. They mainly stem from the calculation of the gradient of $\bar{U}_{\text{EPO}}(l)$ and ∇T . Here, we note that because the statistical temperature fluctuation $(\Delta T)^2 = k_B T^2 / C_v$ [17] of each atom layer is large (because of the small number of atoms per layer), the conventional error estimate of ∇T will be quite large. However, NEAIMD consistently yields a stable temperature profile after a sufficiently long simulation time. Thus, we adopt the error in the linear fitting for ∇T . We also note that the aforementioned nonlinear phenomenon of the gradient of $\bar{U}_{\text{EPO}}(l)$ can also lead to large error bars. The details of the error-bar analysis can be found in SI Sec. 6.

In Fig. 3(d), our results show that κ_{el} indeed dominates the thermal transport process in metals. To compare our results with those of the traditional BTE method, we also utilize the BoltzTraP software [18] (based on electron energy band theory) to calculate $\frac{\kappa_{\text{el}}}{\tau_{\text{el}}}$. In obtaining κ_{el} , we use the constant relaxation time approximation $\tau_{\text{el}} = 1 \times 10^{-14}$ s [18, 19]. To avoid finite size effects in the calculation of κ_{ph} , we also evaluate κ_{ph} from the BTE method with interatomic force constants obtained from ab initio calculations [20, 21], as implemented in the ShengBTE package [22]. Then, we obtain the total thermal conductivities of the metals via the BTE method by

summing κ_{el} from BoltzTraP and κ_{ph} from ShengBTE. Our NEAIMD method, the traditional BTE method and experimental data are compared in Fig. 3(e). The results demonstrate that our method is superior to the traditional BTE method in predicting the electronic thermal conductivities of metals, especially for Be and Cu at room temperature. Moreover, we observe an interesting phenomenon when calculating the spectral density of VEPO ($S_{\Delta U}$) in Fig. 2(b, d). We perform exponential decay fitting of the autocorrelation function of the VEPO using the formula $y = A\exp(-t/\tau_{\text{exp}})$. Surprisingly, the exponential autocorrelation time of VEPO τ_{exp} at room temperature is on the same approximate order of magnitude as the theoretical collision time of the free electrons [18, 19, 23]. The results for Cu and Al are shown in Fig. 3(a). We also examine other metals (Be, Li, and Mg) and obtain similar results (SI Sec. 8). Therefore, we anticipate that some physical mechanisms must drive this phenomenon, i.e., it is not a coincidence.

In summary, we have developed a new methodology based on the concept of EPO to predict the electronic thermal conductivities of metals via direct NEAIMD simulation. Without explicitly addressing any complicated scattering processes of free electrons, our NEAIMD-EPO method provides better predictions of the electronic thermal conductivities of pure metals than the traditional BTE method near room temperature. We expect that this methodology will be helpful and useful for understanding and studying the heat-transfer problems of metal systems in the future. Further extension to cope with some presently challenging problems in materials, such as electron-phonon coupling, is also foreseen.

Acknowledgments

M.H. gratefully acknowledges Prof. David G. Cahill (University of Illinois at Urbana-Champaign) for valuable comments on the manuscript. S.Y.Y. gratefully thanks Dr. Yang Han (RWTH Aachen University) and

Dr. Tao Ouyang (Xiangtan University) for their helpful and fruitful discussions, and Dr. Shi-Ju Ran (ICFO, Spain) for his help in plotting Figs. 1(b, e). X.Z. greatly acknowledges Dr. Zhiwei Cui (Northwestern University) for providing the input script and MEAM potential files for the EMD simulations of Li. The authors gratefully acknowledge the computing time granted by the John von Neumann Institute for Computing (NIC) and provided on the supercomputer JURECA at Jülich Supercomputing Centre (JSC) (Project ID: JHPC25). The classical NEMD and EMD simulations were performed with computing resources granted by the Jülich Aachen Research Alliance-High Performance Computing (JARA-HPC) from RWTH Aachen University under project No. jara0135. S.S. was supported by NERC grant number NE/K006290/1.

Author Contributions

M.H. and S.Y.Y. conceived the project. M.H. supervised the project and E.D.N. co-supervised the project. S.Y.Y. developed the methodology and theoretical formula. S.Y.Y. designed and executed all the AIMD simulations and calculations of the electronic thermal transport properties. G.Q., X.Z. and S.Y.Y. post-processed and analyzed the simulation data. X.Z. and S.Y.Y. performed the frequency domain analysis. S.S. provided the original code of NEAIMD. X.Z. and S.Y.Y. improved the NEAIMD code. S.Y.Y. calculated the thermal conductivity of metals with the BTE method. S.Y.Y., X.Z., E.D.N., S.S. and M.H. co-wrote the manuscript. All authors participated in the discussions and reviewed and revised the manuscript.

Additional Information

Competing financial interests: The authors declare no competing financial interests.

-
- [1] Kittel, C. Introduction to Solid States Physics (8th Ed.). Ch.6, (John.Wiley & Sons, Inc., USA, 2004).
 - [2] Jones, W. & March, N. H. Theoretical Solid State Physics. (Courier Dover Publications, 1985).
 - [3] Desjarlais, M. P., Kress, J. D. & Collins, L. A. Electrical conductivity for warm, dense aluminum plasmas and liquids. *Phys. Rev. E* **66**, 025401(R) (2002).
 - [4] Pozzo, M., Davies, C., Gubbins, D. & Alfè, D. Thermal and electrical conductivity of iron at Earth's core conditions. *Nature* **485**, 355-358 (2012).
 - [5] de Koker, N., Steinle-Neumann, G. & Vlček, V. Electrical resistivity and thermal conductivity of liquid Fe alloys at high P and T, and heat flux in Earth's core. *Proc. Natl. Acad. Sci. USA* **109**, 4070-4073 (2012).
 - [6] Zhang, P., Cohen, R. E. & Haule, K. Effects of electron correlations on transport properties of iron at Earth's core conditions. *Nature* **517**, 605-607 (2015).
 - [7] Stackhouse, S., Stixrude, L. & Karki, B. B. Thermal Conductivity of Periclase (MgO) from First Principles. *Phys. Rev. Lett.* **104**, 208501 (2010).
 - [8] Kim, H., Kim, M. H. & Kaviani, M. Lattice thermal conductivity of UO_2 using ab-initio and classical molecular dynamics. *J. Appl. Phys.* **115**, 123510 (2014).
 - [9] Kresse, G. & Furthmüller, J. Efficient iterative schemes for ab initio total-energy calculations using a plane-wave basis set. *Phys. Rev. B.* **54**, 11169-11186 (1996).
 - [10] Kresse, G. & Furthmüller, J. Efficiency of ab-initio total energy calculations for metals and semiconductors using a plane-wave basis set. *Comput. Mater. Sci.* **6**, 15-50 (1996).
 - [11] Müller-Plathe, F. A simple nonequilibrium molecular dynamics method for calculating the thermal conductivity.

- J. Chem. Phys. **106**, 6082-6085 (1997).
- [12] Dennis, W. R. Echo Signal Processing. (Springer, 2003).
 - [13] Storch, H. V. & Zwiers, F. W. Statistical Analysis in Climate Research. (Cambridge University Press, 2001).
 - [14] Zhang, X. & Jiang J. Thermal conductivity of zeolitic imidazolate framework-8: a molecular simulation study. J. Phys. Chem. C. **117**, 18441-18447 (2013).
 - [15] Taylor, J. R. An Introduction to Error Analysis: the Study of Uncertainties in Physical Measurements (2nd Ed.). Ch.4, (University Science Books, 1997).
 - [16] Ku, H. H. Notes on the use of propagation of error formulas. Journal of Research of the National Bureau of Standards - C. Engineering and Instrumentation, **70C**, No. 4 (1966).
 - [17] Landau, L. D. & Lifshitz, E. M. Statistical Physics, Part 1 (3rd Ed.). Ch.2, (Pergamon Press, 1980).
 - [18] Madsen, G. K. H. & Singh, D. J. BoltzTraP. A code for calculating band-structure dependent quantities. Comput. Phys. Commun. **175**, 67-71 (2006).
 - [19] Chen, M. X. & Podloucky, R. Electronic thermal conductivity as derived by density function theory. Phys. Rev. B **88**, 045134 (2013).
 - [20] Broido, D. A., Malorny, M., Birner, G., Mingo, N. & Stewart, D. A. Intrinsic lattice thermal conductivity of semiconductors from first principles. Appl. Phys. Lett. **91**, 231922 (2007).
 - [21] Lee, S., Esfarjani, K., Mendoza, J., Dresselhaus, S. & Chen, G. Lattice thermal conductivity of Bi, Sb, and Bi-Sb alloy from first principles. Phys. Rev. B. **89**, 085206 (2014).
 - [22] Li, W., Carrete, J., Katcho, N. A. & Mingo, N. Sheng-BTE: A solver of the Boltzmann transport equation for phonons. Comput. Phys. Commun. **185**, 1747-1758 (2014).
 - [23] Campillo, I., Pitarke, J. M., Rubio, A., Zarate, E., & Echenique, P. M. Inelastic lifetimes of hot electrons in real metals. Phys. Rev. Lett. **83**, 2230-2233 (1999).

Supplementary Information for

Methodology for determining the electronic thermal conductivity of metals via direct non-equilibrium ab initio molecular dynamics

Sheng-Ying Yue,¹ Xiaoliang Zhang,² Stephen Stackhouse,³ Guangzhao Qin,² Edoardo Di Napoli,^{1, 4} and Ming Hu^{1, 2, *}

¹*Aachen Institute for Advanced Study in Computational Engineering Science (AICES), RWTH Aachen University, 52062 Aachen, Germany*

²*Institute of Mineral Engineering, Division of Materials Science and Engineering, Faculty of Georesources and Materials Engineering, RWTH Aachen University, 52064 Aachen, Germany*

³*School of Earth and Environment, University of Leeds, Leeds LS2 9JT, United Kingdom*

⁴*Jülich Supercomputing Centre, Forschungszentrum Jülich and JARA-HPC, 52425 Jülich, Germany*

* Author to all whom correspondence should be addressed. E-Mail: hum@ghi.rwth-aachen.de

1. NEAIMD simulation step

All AIMD simulations are performed using the DFT method implemented in VASP [1, 2]. The Perdew-Burke-Ernzerhof parameterization of the generalized gradient approximation (GGA) is used for the exchange-correlated functional [3], and the projector-augmented wave method is applied to model the core electrons [4, 5]. For the energy cut-off, we use the default value in the pseudopotential file. We first relax the system with the NpT -ensemble (constant number of particles, pressure, and temperature) at room temperature to obtain the lattice constants of the metals at a finite temperature. We then apply the resulting lattice constants to construct the initial structures for subsequent NEAIMD simulations.

The NEAIMD simulations are performed using a modified version of the VASP code [6] with the NVE ensemble (constant volume and no thermostat). We apply a fixed boundary condition along the direction of the heat flux and periodic boundary conditions in the two lateral directions (perpendicular to the direction of the heat flux) of the simulation model (see Fig. 1(c) in the main article). To avoid self-interaction between periodic images of the simulation cell, in the direction of the heat flux, we add a vacuum layer with a thickness exceeding 5 \AA on the external sides of the fixed atom layers. The total distance between the periodic images of the simulation model exceeds 10 \AA in real space. The layers next to the fixed layers are the heat-source and heat-sink. A constant atomic heat flux is imposed by applying the Müller-Plathe algorithm [7]. The coldest atom in the hot region and the hottest atom in the cold region are selected, and their kinetic energies (atomic velocities) are exchanged every 50 fs with a 1-fs time step. This operation induces a steady heat-energy-flux in the system and a corresponding temperature gradient (∇T) after running for a sufficiently long time. The energy-exchange time interval is used to control the temperature gradient's magnitude. The linear portion of the temperature gradient lies between the heat baths. By linear fitting the statistically averaged temperatures of each atom layer, we obtain ∇T , which is used to calculate the final electronic thermal conductivity (κ_{el}) and phonon thermal conductivity (κ_{ph}).

For Li, Al and Cu, the size of simulation model is $2 \times 2 \times 8$ conventional cells (16 atom layers along the heat flux direction). For Be and Mg, the size of the simulation model is $2 \times 4 \times 8$ primitive cells (16 atom layers along the heat flux direction). To study size effects, we examine models with a length of 24 atom layers for each metal, i.e., $2 \times 2 \times 12$ conventional cells for Li, Al and Cu and $2 \times 4 \times 12$ primitive cells for Be and Mg. For Al, we also investigate the size effect of the cross-section using a model with $4 \times 4 \times 8$ conventional cells. All the simulation temperatures are approximately 300 K. The basic information for all NEAIMD simulations is presented in Table 1. Additionally, a short movie of the NEAIMD of Cu is given to show the real simulation process.

Table 1: Details of NEAIMD simulation of metals

System	System length (Å)	Cross-sectional area (S, Å ²)	Atom number	Total simulation time (t, ps)	Average temperature (T, K)	ID of simulation cases
Li	38.9160	74.7983	128	100	288.20	Li-1
					293.08	Li-2
					303.64	Li-3
					305.35	Li-4
					313.87	Li-5
					316.28	Li-6
Be	45.8631	36.0108	192	70.503	278.02	Be-1
	31.7520		128	92.206	285.00	Be-2
				95.996	296.17	Be-3
				95.320	311.22	Be-4
				95.907	313.46	Be-5
Mg	47.2410	70.2266	128	64.906	290.95	Mg-1
	68.2388		196	65.178	297.74	Mg-2
				53.513	302.19	Mg-3
				64.520	307.87	Mg-4
				47.2410	128	63.368
Al	52.5067	65.2525	192	51.958	284.48	Al-1
	36.3510		128	76.497	286.14	Al-2
				75.340	299.46	Al-3
				77.251	306.84	Al-4
				71.534	310.39	Al-5
				73.971	318.31	Al-6
Cu	47.0096	52.3134	196	13.424	285.31	Cu-1
	32.5440		128	22.280	293.86	Cu-2
				22.787	298.49	Cu-3
				22.719	310.91	Cu-4

2. PSD and the autocorrelation function

The power spectrum $S_x(f)$ of a time series $x(t)$ describes the distribution of the frequency components composing that signal. According to Fourier analysis, any physical signal can be decomposed into a number of discrete frequencies or a continuous spectrum of frequencies. The statistical average of a certain signal or signal type (including noise), analysed regarding its frequency content, is called its spectrum [8, 9].

The autocorrelation function of a real stationary signal $x(t)$ is defined as

$$R_x(\tau) = E[x(t)x(t + \tau)], \quad (1)$$

where $E[\cdot]$ is the expected value operator. The Fourier transform of $R_x(\tau)$ is called the PSD $S_x(f)$ [8, 9]

$$S_x(f) = \int_{-\infty}^{\infty} R_x(\tau) e^{-2\pi i f \tau} d\tau. \quad (2)$$

Given any two frequencies f_1 and f_2 , the quantity

$$\int_{f_1}^{f_2} S_x(f) df \quad (3)$$

represents the portion of the average signal power contained in the signal frequencies from f_1 to f_2 , where S_x is a spectral density.

Here, to demonstrate the relationship between lattice vibration (i.e., thermal motion of the ion cores) and EPO at the ion cores, we consider the following four physical signals:

- 1) The displacement of the ion cores $D_{ion}(t)$. We extract the position of each ion core from the AIMD run at each time step from the VASP output file. Here, we are particularly interested in the \bar{z} component, i.e., that along the direction of the heat flux. By applying the PSD technique, we obtain the spectral density of atomic displacement (S_D), which gives information regarding atomic vibrations in real space.
- 2) The velocity of the ion cores $V_{ion}(t)$. We modified the VASP code to output the instantaneous velocity of each ion core at every AIMD time step. Analogous to $D_{ion}(t)$, here, we take the \bar{z} component for $V_{ion}(t)$. By applying the PSD technique we obtain the spectral density of atomic velocity (S_V). S_V is conventionally known as the vibrational density of states (VDOS) and provides information regarding the oscillation velocity of the atoms.
- 3) The EP displacement at the ion cores $U_{ion}(t)$. We extract the EP value at each ion core at every AIMD time step from the VASP output file. By applying the PSD technique, we obtain the spectral density of EP displacement (S_U). Based on its definition, S_U reflects the behaviour of EPO at the ion core in real space.
- 4) The VEPO at the ion cores $\Delta U_{ion}(t)$. We define $\Delta U_{ion}(t)$ as the difference between $U_{ion}(t)$ at time step $t + 1$ and t . By applying the PSD technique, we obtain the spectral density of VEPO ($S_{\Delta U}$). Similar to S_V (VDOS), $S_{\Delta U}$ provides information about the rate of the EP value change at the ion core.

The EP expression used in VASP is defined as

$$U = \int U(r) \cdot \rho_{test} \cdot (|r - R|) d^3r, \quad (4)$$

where the test charge ρ_{test} is norm 1. From this formula, we can see that the EP U is a function of ion position R . Thus, the EPO at the ion core is induced by the lattice vibrations, i.e., the thermal motion of the ion cores. Therefore, in principle, S_D and S_U should have some correlation, similar to S_V and $S_{\Delta U}$.

To prove our conjecture, for a selected model of Al, we performed an additional 10-ps equilibrium AIMD simulation with the *NVE* ensemble. The results are shown in Fig. 2(a, b) in the main text. Clearly, the distributions of S_D and S_U and of S_V and $S_{\Delta U}$ are very similar, and the locations of the peaks, with respect to frequency, are in exact agreement. These results strongly support our conjecture. Similarly, the same quantities were determined via a 100-ps NEAIMD

simulation of Al (Fig. 2(c, d)), which revealed a strong correlation between the lattice vibration and the EPO at the ion cores. However, we also note that for some specific frequencies (3.5~5.0 THz), the peaks of the spectral density from the lattice vibration and EPO in Figs. 2(c, d) are not exactly the same. We suspect that this phenomenon may be attributable to the heat flux applied in NEAIMD. Nevertheless, comparing the PSD results confirms that the relationship between lattice vibration and EPO holds.

3. Evidence for the EPO from lattice vibrations providing the thermal kinetic energy to thermally excited electrons

We first give a detailed derivation of the total energy expression for a free electron system at $T > 0$ K.

From the Sommerfeld expansion [10], if the function $Q(E)$ is continuously differentiable on $(-\infty, +\infty)$, $Q(0) = 0$, and $\lim_{E \rightarrow \infty} e^{-\alpha E} Q(E) = 0$ (here, α is a positive and constant number) when $k_B T \ll E_F$, then

$$I = \int_0^\infty f(E) Q'(E) dE \approx Q(E_F) + \frac{\pi^2}{6} (k_B T)^2 Q''(E_F), \quad (5)$$

where $f(E)$ is the Fermi-Dirac distribution function, E_F is the Fermi energy, k_B is the Boltzmann constant and T is the system temperature.

When $T > 0$ K, the total energy of the free electron system U_{sys} can be written as

$$\begin{aligned} U_{sys} &= \int_0^\infty E f(E) N(E) dE \\ &= \int_0^{E_F} E N(E) dE + \frac{\pi^2}{6} (k_B T)^2 \frac{d}{dE} [E N(E)]_{E_F} \\ &= \int_0^{E_F^0} E N(E) dE + \int_{E_F^0}^{E_F} E N(E) dE + \frac{\pi^2}{6} (k_B T)^2 \cdot \frac{3}{2} \left(\frac{1}{2\pi^2} \left(\frac{2m_e}{\hbar^2} \right)^{\frac{3}{2}} \cdot \sqrt{E} \right) \\ &\approx E_0 + E_F^0 N(E_F^0) (E_F - E_F^0) + \frac{\pi^2}{4} (k_B T)^2 N(E_F^0). \\ &\because E_F = E_F^0 \left[1 - \frac{\pi^2}{12} \left(\frac{k_B T}{E_F^0} \right)^2 \right] \text{ and } N(E_F^0) = \frac{3N}{2E_F^0} \\ &\therefore U_{sys} = \int_0^{E_F^0} E N(E) dE + N(E_F^0) \left[-\frac{\pi^2}{12} (k_B T)^2 \right] + \frac{\pi^2}{4} (k_B T)^2 N(E_F^0) \\ &= \int_0^{E_F^0} E N(E) dE + \frac{\pi^2}{6} (k_B T)^2 N(E_F^0) \\ &= E_0 + \frac{\pi^2}{4} \cdot N \frac{(k_B T)^2}{E_F^0}. \end{aligned} \quad (6)$$

The first term (E_0) on the right-hand side of Equation (6) is the total energy of the free electron system at 0 K, whereas the second term is the thermally excited energy (E_T) of the system obtained from the outside environment when $T > 0$ K. Here, N is the total number of free electrons, and E_F^0 is the Fermi energy at 0 K. Because the Fermi energy changes very little with temperature, here, we take E_F at room temperature as E_F^0 [11].

In Fig. 2(f) of the main text, we demonstrate that the local vibrational EP field, which originates from the EPO, causes the collective vibration of free electrons in the momentum space and provides additional thermal kinetic energy to the thermally excited electrons near the Fermi surface. To confirm this, we perform two additional equilibrium AIMD simulations: Al (100 ps at 329.40 K) and Li (100 ps at 283.97 K). Both use a supercell of $2 \times 2 \times 2$ conventional cells (32 atoms in total) and periodic boundary conditions in all three dimensions.

We define the total energy provided by EPO as

$$E_{EPO} = \sum_i 2 \cdot \bar{U}_i \cdot n_i(e), \quad (7)$$

where \bar{U}_i is the average effective amplitude of EPO at the ion core i . Because the simulations here are equilibrium AIMD, the \bar{U}_i of different atoms can be taken as having the same value (over a long time average, the temperature of each ion core can be assumed to be the same). $n_i(e)$ is the number of free electrons per atom (for Al, $n_i(e)=3$; for Li, $n_i(e) = 1$). Then,

$$E_{EPO} = \sum_i 2 \cdot \bar{U}_i n_i(e) = 2 \cdot \bar{U}_{EPO} \sum_i n_i(e) = 2 \cdot \bar{U}_{EPO} \cdot N, \quad (8)$$

where N is the total number of free electrons in the system and \bar{U}_{EPO} is the average effective amplitude of EPO from equilibrium AIMD

$$\bar{U}_{EPO} = \frac{1}{N_a} \sum_{j=1}^{N_a} \sqrt{\frac{1}{n_{steps}} \sum_{t_i}^{n_{steps}} (U_j(t_i) - \bar{U}_j)^2}, \quad (9)$$

where N_a is the total number of atoms in the simulation cell, n_{steps} is the total simulation steps, $U_j(t_i)$ is the EP value of atom j in the cell at time step t_i , and \bar{U}_j is the average EP value of atom j . \bar{U}_{EPO} is calculated using the RMS method [12]. E_T and E_{EPO} for Al and Li are compared in Table 2.

Table 2: Comparison of E_T and E_{EPO} for Al and Li from equilibrium AIMD simulations near room temperature

System	Temperature (K)	Total number of free electrons	Fermi energy (eV)	Average effective amplitude of EPO (10^{-5} V)	Thermally excited energy U_T (10^{-21} J)	Total energy provided by EPO E_{EPO} (10^{-21} J)
Li	283.97	32	4.72	15.5152	1.6049	1.5909
Al	329.40	96	11.63	8.9964	2.6293	2.7674

From the results in Table 2, the following relationship is clear

$$E_T \approx E_{EPO}. \quad (10)$$

This result supports our conjecture that EPO causes the collective vibration of free electrons in momentum space and provides the thermal kinetic energy of the thermally excited electrons.

4. Heat flux via free electrons \vec{J}_{el}

4.1 Results of the EPO in space

As shown in Figs. 2(g, h) of the main text, higher temperatures can increase the strength and speed of spatial EPO. Figs. 2(i, j) in the main text confirm this. From Fig. 2(i), we also have

$$\sum_{j=1}^{N_{al}} \sum_t \Delta U_j(t) \cong 0. \quad (11)$$

Therefore, no net local electric field occurs over the simulation. In other words, no net electric current exists in metals during the heat-transfer process, in good agreement with our common sense arguments. We also note that both the negative and positive parts of $\sum_{j=1}^{N_{al}} \sum_t \Delta U_j(t)$ exhibit perfect linear behaviours with time, as shown in Fig. 2(i). We apply the RMS method to calculate the average effective amplitude of EPO (\bar{U}_{EPO})

$$\bar{U}_{EPO}(l) = \frac{1}{N_{al}} \sum_{j=1}^{N_{al}} \sqrt{\frac{1}{n_{steps}} \sum_{i=1}^{n_{steps}} (U_j(t_i) - \bar{U}_j)^2}, \quad (12)$$

where l is the index of the atom layers, N_{al} is the total number of atoms per layer, n_{steps} is the total number of simulation steps, $U_j(t_i)$ is the EP displacement of ion core j at i fs, and \bar{U}_j is the average value of $U_j(t_i)$ for atom j in layer l . $\bar{U}_{EPO}(l)$ represents the intensity of the local EPO. Thus, the energy provided by EPO in each layer $E_{EPO}(l)$ can be written as

$$E_{EPO}(l) = 2 \cdot \bar{U}_{EPO}(l) \cdot n(e) \cdot e \quad (13)$$

4.2 The distribution of thermally excited electrons' thermal kinetic energy along the heat flux direction and the non-linear effect analysis

We have proven that the energy from EPO provides the kinetic energy of thermally excited electrons. Therefore, we can treat E_{EPO} as the thermal kinetic energy of thermally excited electrons. Combining Eqs. (12) and (13), we present the distribution of the effective amplitude of EPO in space rather than that of the thermal kinetic energy of thermally excited electrons, in Fig. S1.

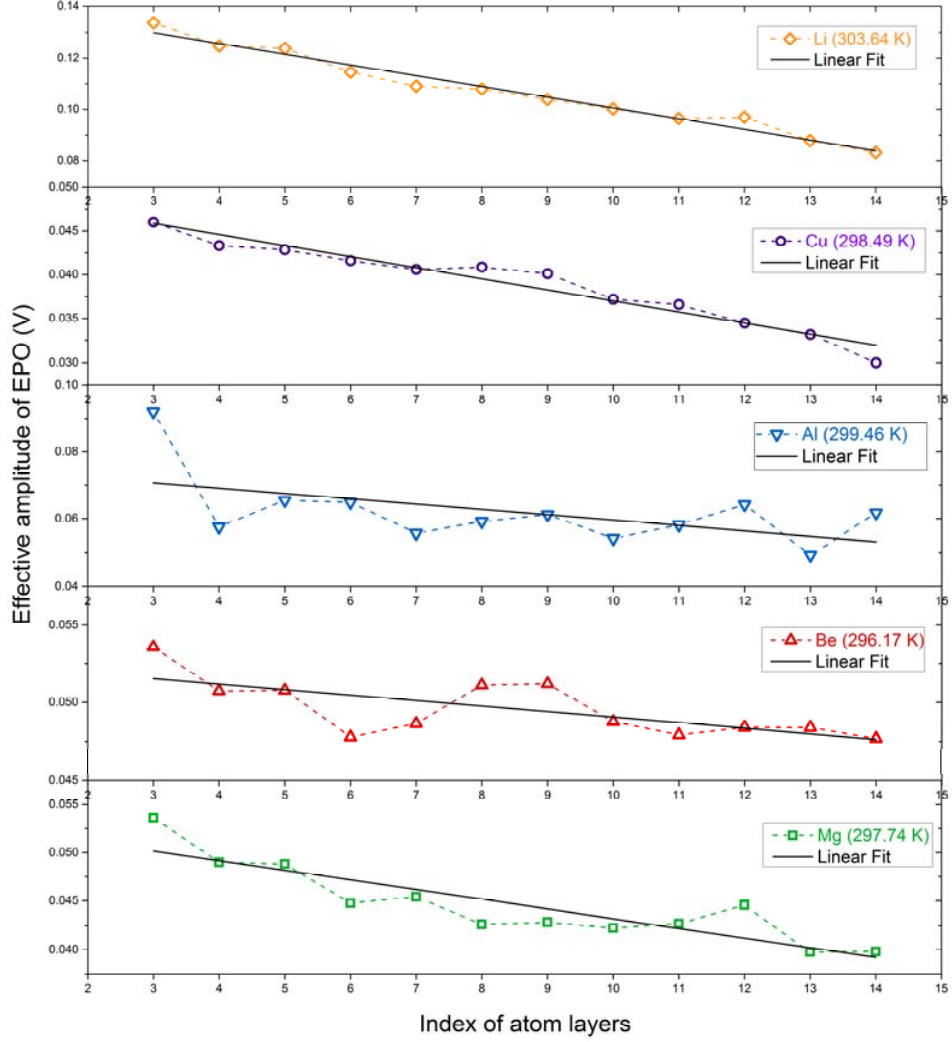


Fig. S1: Effective amplitudes of the EPO along the direction of the heat flux in different metals (all systems are approximately 300 K). Via linear fitting, we can obtain $\frac{\partial \bar{U}_{EPO}(l)}{\partial N_l}$, which is used to calculate electronic heat flux.

Fig. S1 shows that in metals, higher temperatures increase the strength of EPO. We also note that a non-linear phenomenon of $\bar{U}_{EPO}(l)$ occurs in some metals, such as Al, Be. This phenomenon will cause significant errors in the final electronic thermal conductivity (κ_{el}).

To elucidate the reason for this non-linear phenomenon, we plot the temperature profiles of different metals in Fig. S2. The degrees of the non-linear temperature distributions of Be and Al are larger than those of Li, Cu, and Mg at approximately 300 K. The non-linear temperature distribution may be responsible for the non-linear distribution of $\bar{U}_{EPO}(l)$.

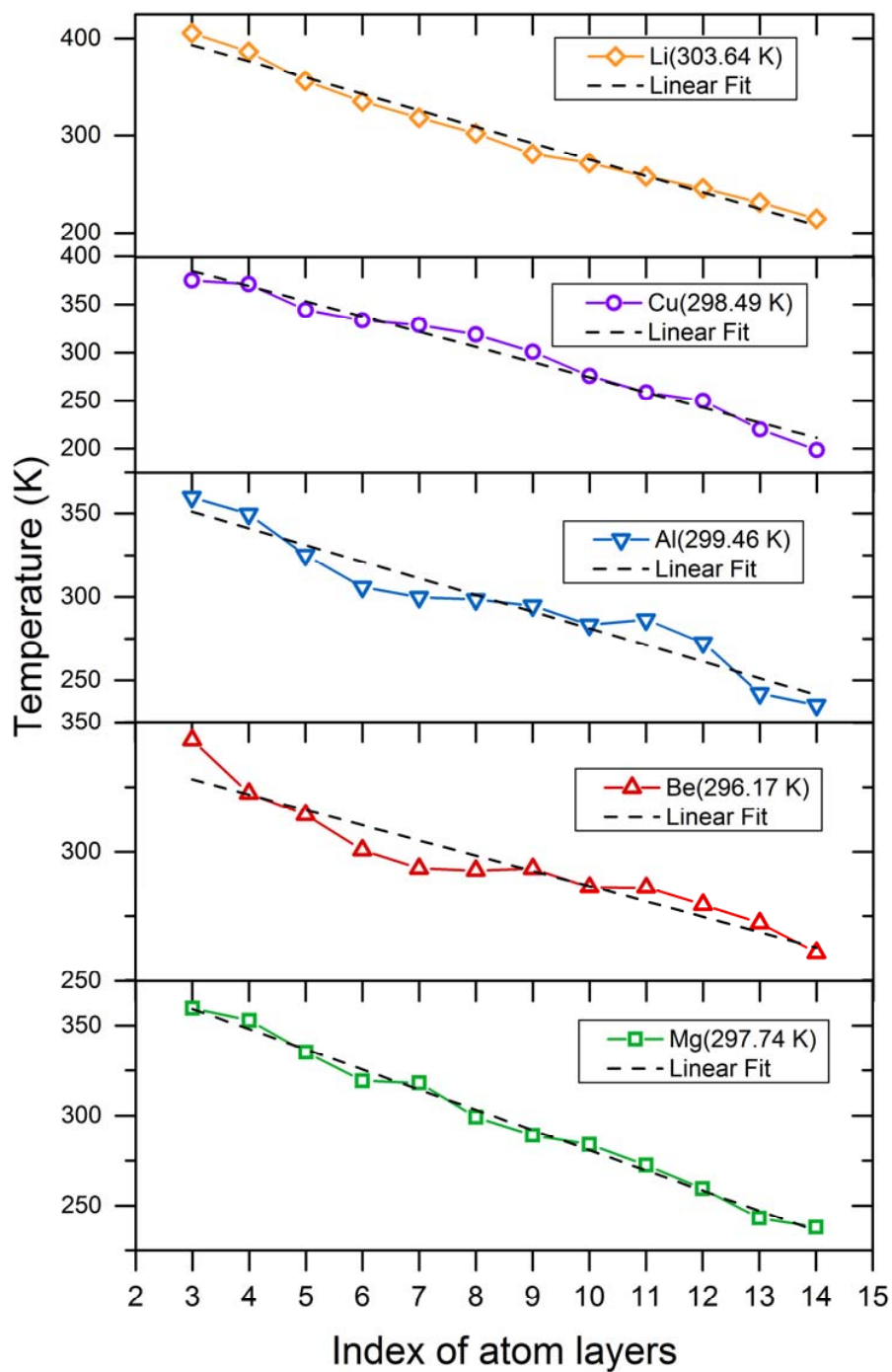


Fig. S2: Temperature profiles from NEAIMD simulations of different metals (all systems are at approximately 300 K). The dashed line is the linear fit of the temperature profile, i.e., the temperature gradient (∇T).

We also attempt to reduce the non-linear effect by increasing the model size. Specifically, we vary the sizes of the Be and Al models. Fig. S3 presents the non-linear effects of different Be lengths at approximately 300 K. Fig. S4 shows the non-linear effects of different cross-sections and lengths of Al at approximately 300 K. Based on these results, the simulation size indeed affects the non-linear EPO phenomenon in metals, and the non-linear effects of EPO along the heat flux direction can be reduced by increasing the simulation size. However, we could not completely eliminate the non-linear effects by increasing the simulation size. The mechanism underlying this non-linear phenomenon warrants further study.

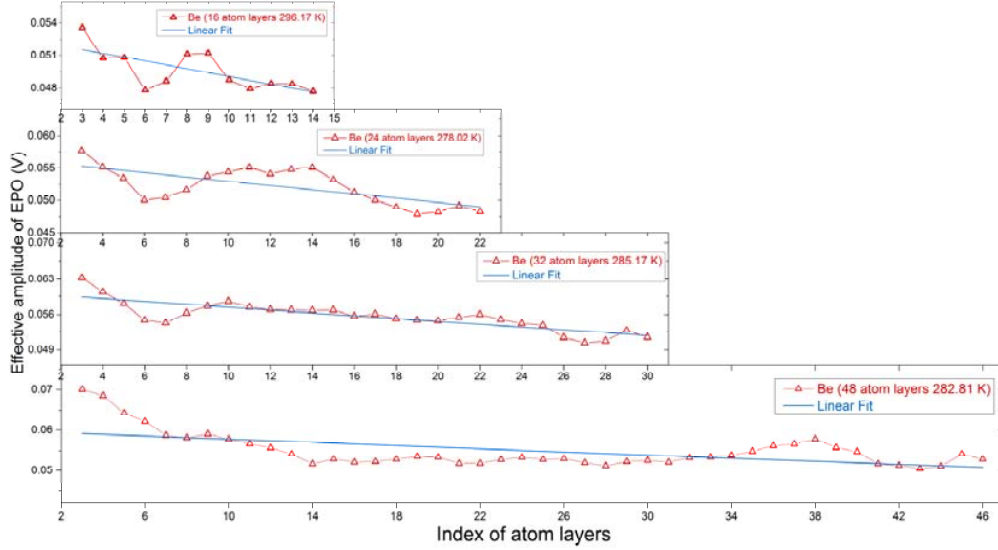


Fig. S3: Distributions of the effective EPO amplitude for different lengths of Be (all systems are at approximately 300 K).

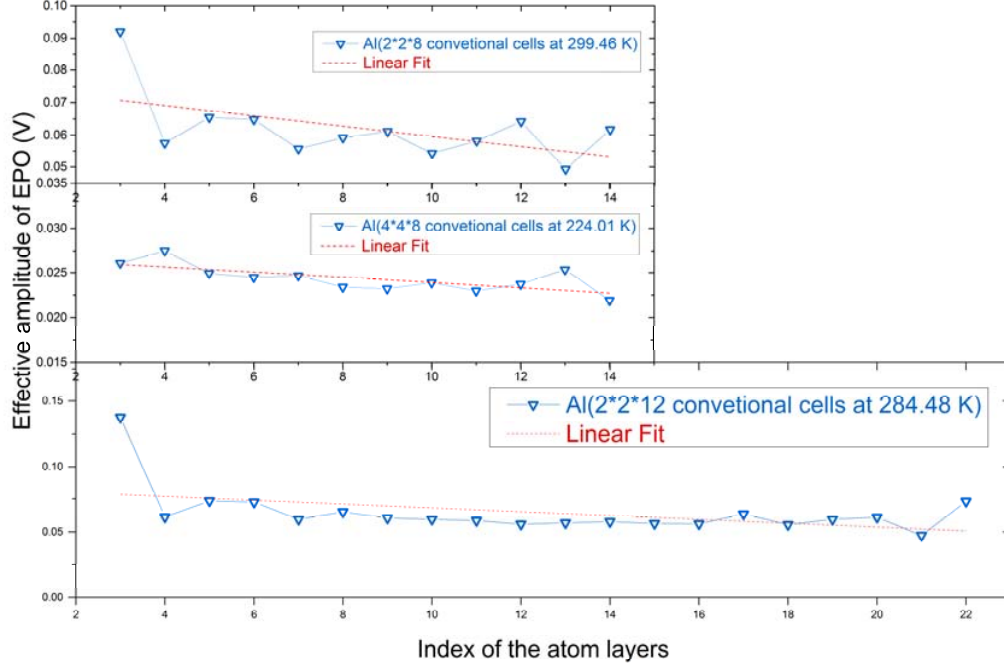


Fig. S4: Distributions of the effective EPO amplitude for different cross-sections and lengths of Al (all systems are at approximately 300 K).

4.3 Definition of \vec{J}_{el}

First, we calculate the average effective EPO amplitude $\bar{U}_{EPO}(l)$ and effective EPO energy $E_{EPO}(l)$. Then, we can obtain the total effective energy provided by EPO during simulation time t as

$$E_{EPO}(l, t) = 2 \cdot \bar{U}_{EPO}(l) \cdot n(e) \cdot e \cdot n_{steps}, \quad (14)$$

where n_{steps} is the total number of time steps during the simulation time t . When the system reaches a quasi-equilibrium state, we can infer that the thermal energy of thermally excited electrons is exchanged between two adjacent atom layers. As illustrated in Fig. S5, we take half of the difference of the thermal kinetic energy exchange between the two layers as \vec{J}_{el} (because of the isotropy of the free electron model)

$$\begin{aligned} \vec{J}_{el} &= -\frac{1}{2} \frac{n(e) \cdot e \cdot \partial [2 \cdot \bar{U}_{EPO}(l) \cdot n_{steps}]}{S \cdot t \cdot \partial N_l} \\ &= -\frac{n(e) \cdot e \cdot n_{steps}}{S \cdot t} \frac{\partial \bar{U}_{EPO}(l)}{\partial N_l}, \end{aligned} \quad (15)$$

where S is the cross-sectional area, $n(e)$ is the number of free electrons per atom layer, e is the unit charge of a single electron, and $\frac{\partial \bar{U}_{EPO}(l)}{\partial N_l}$ is the gradient of the average effective EPO amplitude value by linear fitting of $\bar{U}_{EPO}(l)$ with respect to the index number of atom layers (N_l), as shown in Fig. S1.

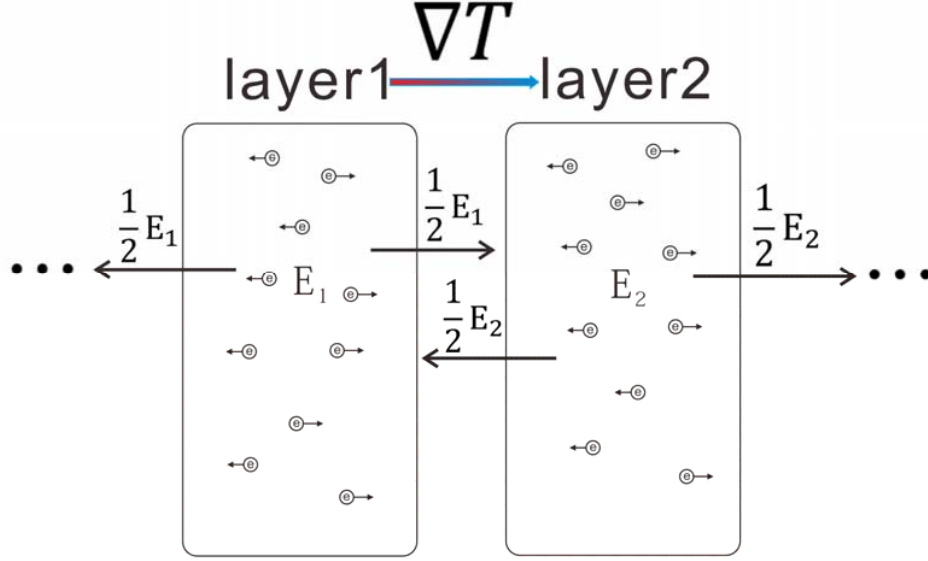


Fig. S5: Schematic of the exchange of thermal excited electrons' thermal energy between two adjacent atom layers. E_1 and E_2 are the thermal energies carried by thermally excited electrons in layer1 and layer2, respectively.

5. Calculation of thermal conductivity κ of metals from NEAIMD

5.1 Electronic thermal conductivity (κ_{el})

From Fourier's Law of heat conduction, the electronic thermal conductivity (κ_{el}) can be written as

$$\kappa_{el} = -J_{el}/\nabla T. \quad (16)$$

Combining Equation (16) with Equation (15), we have

$$\kappa_{el} = \frac{n(e) \cdot e \cdot n_{steps}}{S \cdot t \cdot \nabla T} \frac{\partial \bar{U}_{EPO}(l)}{\partial N_l}. \quad (17)$$

Based on Eq. (17), we calculate the κ_{el} of five metals: Li, Be, Mg, Al, and Cu around room temperature. We run multiple NEAIMD simulations for each system with different T to examine the temperature dependent thermal conductivity of metals. All the simulation results are reported in Table 3.

5.2 Phonon thermal conductivity (κ_{ph})

As we employ the Müller-Plathe algorithm to establish a stable temperature gradient along the heat transfer direction, we can also obtain the atomic kinetic energy flux J_{ph} . We calculated the phonon thermal conductivity (κ_{ph}) simultaneously from Fourier's Law:

$$\kappa_{ph} = -J_{ph}/\nabla T. \quad (18)$$

The results are also reported in Table 3. By summing κ_{el} and κ_{ph} , we obtain the total κ of metals from parameter free NEAIMD simulations.

Table 3: Electronic thermal conductivity κ_{el} and phonon thermal conductivity κ_{ph} from NEAIMD.

System	Case ID	Average temp. (T, K)	Temperature gradient ∇T (K/Å)	Electronic thermal conductivity κ_{el} (W/mK)	Phonon thermal conductivity κ_{ph} (W/mK)	Total thermal conductivity κ (W/mK)
Li	Li-1	288.20	-7.2117	82.1294	2.7502	84.8796
	Li-2	293.08	-7.6875	81.0457	2.6219	83.6676
	Li-3	303.64	-7.7978	79.9341	2.6386	82.5727
	Li-4	305.35	-7.9970	78.4404	2.5930	81.0334
	Li-5	313.87	-8.1606	77.3224	2.6050	79.9274
	Li-6	316.28	-8.2397	76.7194	2.5927	79.3121
Be	Be-1	278.02	-2.2042	220.9939	25.0928	246.0867
	Be-2	285.00	-2.9479	216.3805	21.0501	237.4306
	Be-3	296.17	-3.3623	196.5404	18.8916	215.4320
	Be-4	311.22	-3.8448	174.4980	16.9305	191.4285
	Be-5	313.46	-3.6524	164.2614	18.5753	182.8367
Mg	Mg-1	290.95	-4.8223	166.4749	2.1260	168.6009
	Mg-2	297.74	-4.2645	148.2052	2.4020	150.6072
	Mg-3	302.19	-3.6466	140.7474	2.3877	143.1351
	Mg-4	307.87	-5.8340	140.4684	1.7672	142.2356
	Mg-5	311.41	-5.1873	142.9120	2.0244	144.9364
Al	Al-1	284.48	-3.0485	232.7718	5.7530	238.5248
	Al-2	286.14	-4.9667	231.2791	4.5353	235.8144
	Al-3	299.46	-4.9448	223.9373	4.6760	228.6133
	Al-4	306.84	-5.2123	223.6268	4.6600	228.2868
	Al-5	310.39	-5.3456	220.0350	4.3882	224.4232
	Al-6	318.31	-5.5119	209.5108	4.3312	213.8420
Cu	Cu-1	285.31	-7.2400	438.9252	2.0393	440.9645
	Cu-2	293.86	-9.6536	399.0878	1.8816	400.9694
	Cu-3	298.49	-8.7284	391.4515	2.1829	393.6344
	Cu-4	310.91	-9.9209	374.4141	1.9523	376.3664

5.3 Size effects of lattice thermal conductivity κ_{ph} from NEAIMD

It is well known that, in lattice dynamics each vibrational mode (phonon) has a specific wavelength. In view of this, finite size effects are inevitable in non-equilibrium molecular dynamics (NEMD) simulations of lattice thermal conductivity of most systems, where phonons are truncated due to the limited model length [13].

Due to the computational limitation of the AIMD, here we perform classical NEMD simulations of Cu at 300 K with different simulation cell length along the direction of heat transfer using the LAMMPS [14] package. The Cu-Cu interatomic interactions are described by the embedded-atom-method (EAM) potential [15]. In Fig. S6, we can see the strong finite size effect of κ_{ph} . The length of our NEAIMD model of Cu is 8 unit cells and our NEAIMD result of κ_{ph} is about 2.18 W/mK around 300 K, which is similar to the classical NEMD results (3.84 W/mK) in Fig. S6.

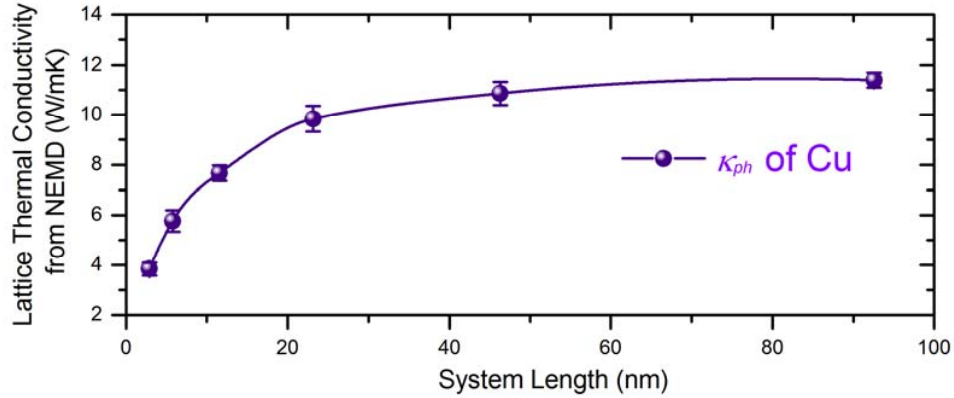


Fig. S6: Size effect of lattice thermal conductivity of Cu from non-equilibrium molecular dynamics simulation around 300 K.

To compare κ_{ph} results from different calculation methods, we first calculate κ_{ph} of different metals, at around 300 K, from classical equilibrium molecular dynamics (EMD) simulations, using the Green-Kubo method [13], as implemented in the LAMMPS package. The EAM potential parameters for Al [16], Cu [15], Be [17], Mg [18] and Li [19] are used to describe the interatomic interactions in the EMD simulations. The results are shown in Fig. S7.

Second, we calculate κ_{ph} of metals at 300 K by solving the phonon Boltzmann transport equation (BTE), with force constants extracted from first-principles calculations. The phonon BTE model does not suffer from finite size effects. We employ the first-principle software package VASP [1,2] to calculate the second-order (harmonic) and third-order (anharmonic) force constants based on the finite displacement difference method [20, 21], and then use the ShengBTE package [21] to obtain κ_{ph} by iteratively solving the BTE of phonons. The convergences of κ_{ph} with respect to the k -grid size ($N \times N \times N$) in our calculations are fully examined and the parameter $N = 20$ is taken to evaluate the converged κ_{ph} . The convergences of κ_{ph} with respect to the force cut-off distance are also examined and we took the distance of the fifth-order adjacent neighbor atoms as the force cut-off. The energy of plane-wave cutoff are adopted the value of 1.5 times of the default value in VASP pseudo-potential files.

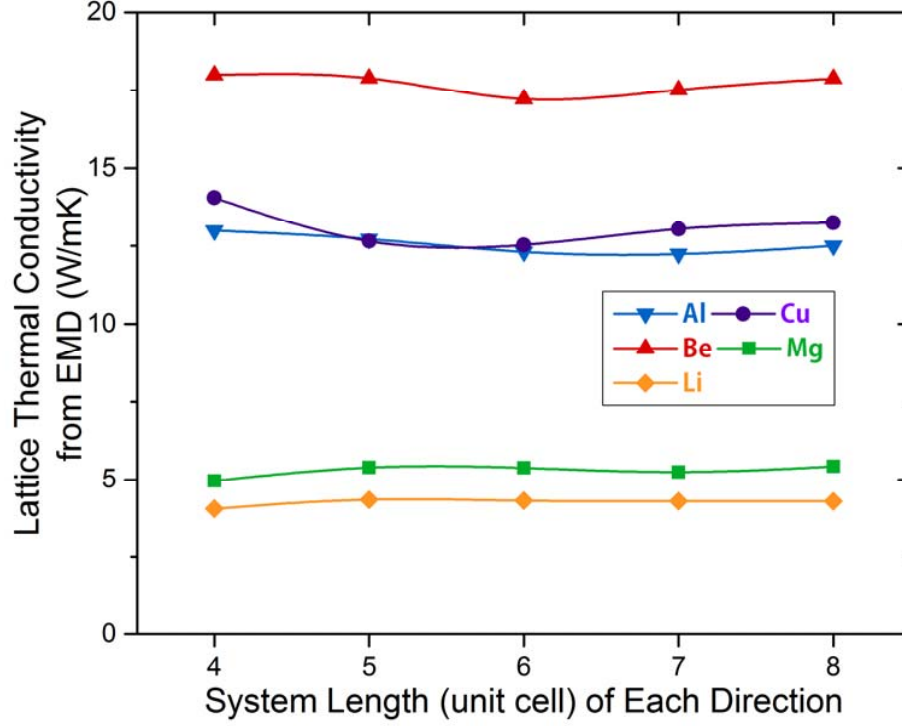


Fig. S7: Size effect of lattice thermal conductivity of metals from equilibrium molecular dynamics simulation around 300 K.

Finally, we compare κ_{ph} from NEAIMD, classical EMD and phonon BTE method in Table 4. It can be seen that our NEAIMD simulations underestimate κ_{ph} of Li, Al, Mg, and Cu. The effect is particularly significant for Cu. However, for Be, κ_{ph} from NEAIMD is a little bit higher than the results from classical EMD and phonon BTE method.

We also examined the relationship between simulation size and non-linear effect for κ_{el} from NEAIMD. The results can be found in Table 1 and Table 3. Unlike κ_{ph} , from our NEAIMD simulations results, we do not observe a clear size effect for κ_{el} .

Table 4. Comparison of lattice thermal conductivity κ_{ph} (at approximately 300 K) calculated by NEAIMD, classical EMD and phonon BTE method.

System	Li	Be	Mg	Al	Cu
NEAIMD κ_{ph} (W/mK)	2.6386	18.8917	2.4021	4.6760	2.1829
Classical EMD κ_{ph} (W/mK)	4.3013	17.8805	5.4244	12.5067	13.2420
BTE κ_{ph} (W/mK)	3.2080	15.2697	8.3925	6.3789	20.4131

6. Analysis of propagation of errors

From the knowledge of the statistical average propagation of errors [22], we know that, when a variable is defined as $X = \frac{u}{v}$, the square of the error in X can be expressed as

$$\begin{aligned}\sigma_X^2 &= \sigma_{\frac{u}{v}}^2 = \sigma_u^2 \left(\frac{\partial X}{\partial u} \right)_{\bar{u}}^2 + \sigma_v^2 \left(\frac{\partial X}{\partial v} \right)_{\bar{v}}^2 = \frac{\sigma_u^2}{\bar{v}^2} + \frac{\sigma_v^2 \bar{u}^2}{\bar{v}^4} \\ &\Rightarrow \left(\frac{\sigma_X}{\frac{\bar{u}}{\bar{v}}} \right)^2 = \left(\frac{\sigma_u}{\frac{\bar{u}}{\bar{v}}} \right)^2 = \left(\frac{\sigma_u}{\bar{u}} \right)^2 + \left(\frac{\sigma_v}{\bar{v}} \right)^2.\end{aligned}\quad (19)$$

From Equations (17) and (19), we know that the error in κ_{el} mainly originates from ∇T and $\frac{\partial \bar{U}_{EPO}(l)}{\partial N_l}$. As the ∇T calculation is based on the statistical time average of temperature of each single atom layer, the temperature fluctuation $\overline{(\Delta T)^2} = k_B T^2 / C_v$ [23] of each layer is large due to the small number of atoms in the layer. Thus, the conventional error estimate for ∇T is quite large. However, from Fig. S2 we find that the NEAIMD always yields a stable temperature profile after sufficient simulation time, and so we have reason enough to assume the linear fitting error as the error in ∇T .

At the same time, we notice that the non-linear phenomenon of $\frac{\partial \bar{U}_{EPO}(l)}{\partial N_l}$, which was discussed in Sec. 4.2, leads to a relatively large error in κ_{el} . We calculate the error in κ_{el} (Table 5) from Equation (19). From Table 5 we can see that the κ_{el} of Be and Al have relatively large uncertainties, because of the large error in $\frac{\partial \bar{U}_{EPO}(l)}{\partial N_l}$.

Table 5. Error bar of electrical thermal conductivity κ_{el} of metals around 300 K.

System	Li	Be	Mg	Al	Cu
Temperature (K)	303.64	296.17	297.74	299.46	298.49
Error bar of linear fitting ∇T	4.06%	10.36%	2.86%	8.57%	4.74%
Error bar of linear fitting $\frac{\partial \bar{U}_{EPO}(l)}{\partial N_l}$	7.15%	27.04%	15.88%	28.61%	7.19%
Total error bar of κ_{el} (W/mK)	6.79	62.38	24.30	67.90	33.88
Total error bar of κ_{el} (percentage)	8.22%	28.96%	16.13%	29.86%	8.61%

7. Comparing our results with conventional BTE method and experimental data

In order to examine our theory and evaluate the results of our method, we compare our simulation results of some common metals with experimental measurements and the results from the traditional BTE framework.

In Sec. 5.3, we calculated the lattice thermal conductivity, κ_{ph} , of metals with the BTE method based on first-principle calculations. From the free electron model and BTE theory, we can estimate the electronic thermal conductivity κ_{el} as [11]

$$\kappa_{el} = \frac{\pi^2 n k_B^2 T \tau_{el}}{3m}, \quad (20)$$

where n is the concentration of free electrons, m is the electron mass, k_B is Boltzmann constant, T is system temperature, and τ_{el} is the collision time of free electrons. The value of $\frac{\kappa_{el}}{\tau_{el}}$ is calculated using the BoltzTraP package [24] to solve BTE for electrons based on the electronic band structures, which are calculated by VASP. As in usual practice, we take $\tau_{el} = 1 \times 10^{-14}$ s [24, 25], allowing us to obtain κ_{el} from the conventional BTE framework.

Finally, we get the total thermal conductivity of metals (κ) by summing up the lattice thermal conductivity (κ_{ph}) and electronic thermal conductivity (κ_{el}). The results of κ_{ph} , κ_{el} , and κ from different methods along with the experimental measurement data are reported in Table 6. The comparison clearly shows that our method is much better at predicting the thermal conductivity of metals than the conventional BTE method.

Table 6. Comparison of κ_{ph} , κ_{el} , and κ of simulated metals among our NEAIMD method, conventional BTE method, and experiments at 300 K.

System	NEAIMD κ_{el} (W/mK)	BTE κ_{el} (W/mK)	NEAIMD κ_{ph} (W/mK)	BTE κ_{ph} (W/mK)	NEAIMD total κ (W/mK)	BTE total κ (W/mK)	Exp. κ (W/mK)
Li	79.9341	70.3525	2.6386	3.2080	82.5727	73.5605	84.8
Be	196.5404	48.1385	18.8917	15.2697	215.4321	63.4082	200
Mg	148.2052	105.4915	2.4021	8.3925	150.6073	113.8840	156
Al	223.9373	221.5790	4.6760	6.3789	228.6133	227.9579	237
Cu	391.4515	136.0173	2.1829	20.4131	393.6344	156.4304	401

8. The exponential autocorrelation time of velocity of EPO at ion core

In calculation of the spectral density of electrostatic potential oscillating velocity ($S_{\Delta U}$) in Sec. 2, after calculating the autocorrelation function of velocity of EPO at ion core $\Delta U_{ion}(t)$, we performed an exponential decay fitting of the autocorrelation function with the formula

$$y = A \exp(-t/\tau_{exp}), \quad (21)$$

where τ_{exp} is called the exponential autocorrelation time. It is surprising to find that τ_{exp} is approximately on the same order of magnitude as the collision time of free electrons ($\tau_{el} = 1 \times 10^{-14}$ s). We examined all cases of metals and present the data of τ_{exp} in Table 7. The order of magnitude of our results ($\sim 10^{-14}$ s) agrees very well with the common theoretical value [24-26]. We anticipate that there must be some physical mechanisms behind this phenomenon.

Table 7. Exponential autocorrelation time τ_{exp} of velocity of EPO at ion core (300 K)

System	Li	Be	Mg	Al	Cu
Temperature (K)	302.32	300.67	299.22	299.89	300.72
$\tau_{exp} (\times 10^{-14} \text{s})$	1.258	0.584	1.617	1.282	1.431

9. Advantages, limitations, challenges, and future work of this method

9.1 Advantages

- 1) Our NEAIMD-EPO method provides a direct and clear procedure for simulating the thermal transport behavior of free electrons from an atomistic point of view. It will be very advantageous for investigations of very-large-scale integration (VLSI), of relevance to the semiconductor industry.
- 2) The NEAIMD-EPO method naturally but implicitly includes the complicated interactions between electrons and electron-phonon coupling.
- 3) The NEAIMD-EPO approach is a new method which can calculate electronic thermal conductivity without artificial manipulation and input parameters.
- 4) The NEAIMD-EPO framework also provides the physical picture of how the thermal energy is carried by thermally excited electrons and how this energy is transported in metals.

9.2 Challenges

- 1) The nonlinear phenomenon of the effective amplitude of EPO along the heat flux direction in some metals still needs further study.
- 2) A coherent understanding why the exponential autocorrelation time of velocity of EPO at ion cores has the same order of magnitude as the collision time of free electrons is still missing.

9.3 Limitations

- 1) As our NEAIMD-EPO framework is built on the free electron gas model, so far, this method is limited to simulation of pure metals.
- 2) So far, this method cannot be directly used to simulate thermal transport of metals at low temperatures.
- 3) As this method is realized in the ab initio molecular dynamics simulation, the simulation results will depend on the pseudopotential used.
- 4) The computation costs for the NEAIMD simulations are much higher than that of normal density functional theory (DFT) simulations.

9.4 Future work

With the theory and computational capacity improving, the NEAIMD-EPO method shows the potential in investigating alloys, semiconductors, metal/non-metal interfaces, and even directly simulating nano-devices in the future. It will be promising in theoretical study of the nanotechnology.

